INTERNATIONAL JOURNAL FOR NUMERICAL METHODS IN FLUIDS
Int. J. Numer. Meth. Fluids 2005; **49**:619–633
Published online 14 July 2005 in Wiley InterScience (www.interscience.wiley.com). DOI: 10.1002/fld.1018

Unstructured lattice Boltzmann method in three dimensions

N. Rossi[1], S. Ubertini[1,*,†], G. Bella[1] and S. Succi[2]

[1]*Dipartimento di Ingegneria Meccanica, Università di Roma, Tor Vergata, Via del Politecnico, 1, 00133 Roma, Italy*
[2]*Istituto Applicazioni Calcolo, CNR V.le del Policlinico 137, 00161 Roma, Italy*

SUMMARY

Over the last decade, the lattice Boltzmann method (LBM) has evolved into a valuable alternative to continuum computational fluid dynamics (CFD) methods for the numerical simulation of several complex fluid-dynamic problems. Recent advances in lattice Boltzmann research have considerably extended the capability of LBM to handle complex geometries. Among these, a particularly remarkable option is represented by cell-vertex finite-volume formulations which permit LBM to operate on fully unstructured grids. The two-dimensional implementation of unstructured LBM, based on the use of triangular elements, has shown capability of tolerating significant grid distortions without suffering any appreciable numerical viscosity effects, to second-order in the mesh size. In this work, we present the first three-dimensional generalization of the unstructured lattice Boltzmann technique (ULBE as unstructured lattice Boltzmann equation), in which geometrical flexibility is achieved by coarse-graining the lattice Boltzmann equation in differential form, using tetrahedrical grids. This 3D extension is demonstrated for the case of 3D pipe flow and moderate Reynolds numbers flow past a sphere. The results provide evidence that the ULBE has significant potential for the accurate calculation of flows in complex 3D geometries. Copyright © 2005 John Wiley & Sons, Ltd.

KEY WORDS: fluid dynamics; lattice Boltzmann; finite volumes; unstructured mesh

1. INTRODUCTION

In the last decade lattice Boltzmann methods have undergone a major progress as an alternative to the discretization of the Navier–Stokes equations for the numerical solution of complex fluid problems [1–3]. The original LB method is based on a minimal kinetic Boltzmann equation in which representative particles ('parcels of fluids') evolve on a regular Cartesian grid according to simple streaming and collide rules, designed in such a way as to preserve the basic symmetries (conservation laws) of fluid dynamics. The simplicity of the stream-and-collide dynamics makes LB very efficient from the computational point of view. However, uniform

*Correspondence to: S. Ubertini, Dipartimento di Ingegneria Meccanica, Università di Roma, Tor Vergata, Via del Politecnico, 1, 00133 Roma, Italy.
†E-mail: stefano.ubertini@uniroma2.it

Received 8 August 2004
Revised 18 May 2005
Accepted 23 May 2005

Cartesian grids also represent a severe limitation for many practical engineering problems involving real-life complex geometries, such as cars and airplanes. Therefore, in the recent years, much research has been directed to the goal of enhancing the geometrical flexibility of the LB method. Indeed, starting from the earliest finite-volume formulations more than a decade ago [4], today many options are available to deal with realistically complex geometries [5–9]. A particularly interesting development is represented by finite-volume formulations on fully unstructured grids [10–15]. Unstructured lattice Boltzmann schemes (ULBE) integrate the differential form of the lattice Boltzmann equation (LBE) using a *cell-vertex* finite-volume technique in which the unknown fields are placed at the nodes of the mesh and evolve based on the fluxes crossing the surfaces of the corresponding control volumes. These finite-volume formulations are best viewed as a coarse-grained version of the original LB dynamics, in which geometrical flexibility is achieved at the level of the coarse-graining elements, whose triangular shape (in two dimensions) can accommodate the most complex geometries. To date, ULBE implementations were limited to two-dimensional problems. In this work, we present the first three-dimensional generalization of the ULBE technique.

2. FORMULATION OF UNSTRUCTURED LBE IN THREE DIMENSIONS

The present finite-volume formulation begins with the differential form of the single-time relaxation lattice Boltzmann equation:

$$\partial_t f_i + \mathbf{c}_i \cdot \overrightarrow{\partial}_x f_i = -(f_i - f_i^{\mathrm{eq}})/\tau \tag{1}$$

Here $f_i(\mathbf{x},t) \equiv f(\mathbf{x},\mathbf{v}=\mathbf{c}_i,t)$, $i=1,b$, is the probability of finding a particle at lattice site $\mathbf{x}$ at time t, moving along the lattice direction defined by the discrete speed $\mathbf{c}_i$. The left-hand side of this equation represents the molecular free-streaming, whereas the right-hand side represents molecular collisions via a single-time relaxation towards local equilibrium f_i^{eq} on a typical timescale τ [16]. This local equilibrium is a (local) Maxwellian expanded to second-order in the fluid speed

$$f_i^{\mathrm{eq}} = \rho w_i \left[1 + \beta u_i + \frac{\beta^2}{2}(u_i^2 - u^2)\right] \tag{2}$$

where w_i are weighting factors normalized to unit value, $u_i = \mathbf{u}\cdot\mathbf{c}_i$ and $\beta = 1/c_s^2$, c_s being the lattice sound speed, defined by the equation $c_s^2 = \sum_i w_i c_i^2$, ($c_s = 1/\sqrt{3}$ in the present work).

In the above

$$\rho = \sum_i f_i, \quad \mathbf{u} = \sum_i \mathbf{c}_i f_i/\rho$$

are the fluid density and flow velocity, respectively. Crucial to the LB hydrodynamics is the momentum flux tensor, defined as

$$P = \sum_i \mathbf{c}_i \mathbf{c}_i f_i$$

The equilibrium component of this tensor controls advection and pressure terms, while the non-equilibrium part is in charge of describing dissipative effects.

In the original LB scheme the space-time discretization of the differential equation (1) is performed through an explicit finite differencing along the particle trajectories (straight lines since the discrete speeds are constant). This yields the LBE

$$f_i(\mathbf{x}+\mathbf{c}_i\Delta t, t+\Delta t) = f_i(\mathbf{x},t) - \frac{\Delta t}{\tau}(f_i - f_i^{\mathrm{eq}}) \tag{3}$$

In the limit of weak departures from local equilibrium, i.e. small Knudsen numbers, it can be shown through a Chapman–Enskog analysis [1] that LBE recovers the dynamic behaviour of a fluid with pressure $p=\rho c_s^2$ and kinematic viscosity $\nu = c_s^2(\tau - \Delta t/2)$. In order to recover the correct fluid dynamic equations in the macroscopic limit, the set of discrete speeds must satisfy mass, momentum and energy conservation, as well as rotational symmetry. This amounts to imposing the following constraints on the local equilibrium distribution:

$$\sum_i f_i^{\mathrm{eq}} = \rho$$

$$\sum_i f_i^{\mathrm{eq}} \mathbf{c}_i = \rho \mathbf{u}$$

$$\sum_i f_i^{\mathrm{eq}} \mathbf{c}_i \mathbf{c}_i = \rho \mathbf{u}\mathbf{u} + \rho c_s^2 I$$

It should be noted that the local equilibria fulfilling such relation are second-order polynomials in the velocity field, as opposed to the Maxwellian shape of local equilibria in the continuum. Indeed, it can be shown that a discrete Maxwellian cannot fulfill the above constraints. The result is that LB is limited to quasi-incompressible, low-Mach number flows, $Ma = u/c_s < 0.1$. Even so, only a limited class of lattices exhibits the right symmetry to ensure the conservation constraints.

In the present work we shall refer to the three-dimensional nineteen-speed model (known as D3Q19) defined by the following set of discrete speeds [16]: One zero-speed particle (cell-centre), Six speed-1 particles (cell centre to face centres), Twelve speed 2 particles (cell centre to edge centres), with weights $w_0 = \frac{4}{9}$, $w_1 = \frac{1}{9}$, $w_2 = \frac{1}{36}$, respectively.

The main advantages of LB are its simplicity and amenability to parallel computing. In particular, owing to its kinetic nature, the pressure field and the stress tensor are locally available, with no need of solving any (expensive) Poisson problem. In fact, it is readily checked that the stress tensor S_{ab} is related to the non-equilibrium component of the momentum flux tensor by the following *local* expression: $S_{ab} = \sum_i [c_{ia}c_{ib} - c_s^2\delta_{ab}](f_i - f_i^{\mathrm{eq}})$ $a,\ b = x,y,z$. Another key property of LB is that non-linearities are local (quadratic dependence of the local equilibrium on the flow field) and the non-localities are linear because advection proceeds along constant, straight lines defined by the discrete speeds $\mathbf{c}_i$. This is a very useful property, not shared by the Navier–Stokes equations, in which non-linearity and non-locality come together into the same $u\nabla u$ term, that is, the fluid moves its own momentum along a space-time changing direction defined by the flow speed itself.

However, a recognized weakness of LB is its restriction to regular, uniform lattices (regular Cartesian grids). This limitation is particularly severe whenever high local resolution is required, as is the case for most flows of engineering interest. For instance, curved boundaries must be approximated by staircase profiles aligned with the gridline coordinates, an appro-

ximation which can lead to severe inaccuracies for aerodynamic flows, unless a sophisticated treatment of the boundary is applied [17, 18]. This has motivated a wide body of research aimed at extending the LB method to non-uniform grids with boundary conditions capable of accommodating curved boundaries [4, 5]. Particularly interesting are recent attempts to formulate LB on a fully unstructured grids [10, 11, 13–15] using cell-vertex finite-volume schemes.

To date, these formulations were limited to two-dimensional flows. In this paper, we present the first three-dimensional formulation and implementation of the ULBE method.

3. THREE-DIMENSIONAL LB ON UNSTRUCTURED GRIDS

In our approach the space discretization of the differential LBE (1) is performed by introducing a tessellation based on tetrahedral elements. To each node P of the discrete grid, we associate a set of $b=19$ discrete populations $f_i(P,t)$, $i=0,18$, which represent the unknowns of the problem. The set of K tetrahedra $T_k(P)$, $k=1,K$, (see Figure 1) which share P as a common vertex defines the finite volume $T(P)$ associated with node P. In the above, the connectivity K is free to change from node to node.

Each of these K tetrahedra is defined by four vertices $\{P,N_j\}$, four triangular surfaces, three of which S_h share P as a common vertex, and six edges, three of which E_m emanate from vertex P. The point O_k is the centre of the tetrahedron T_k, E_m are the midpoints of the edges E_m and S_{jl} are the centres of surfaces S_h, identified by nodes $\{P,N_j,N_l\}$.

Application of the Gauss theorem to each finite volume Ω_k yields the following set of ordinary differential equations:

$$\partial_t f_i(P,t)=\frac{1}{V_P}\sum_k(\Phi_{ik}-\Xi_{ik}) \tag{4}$$

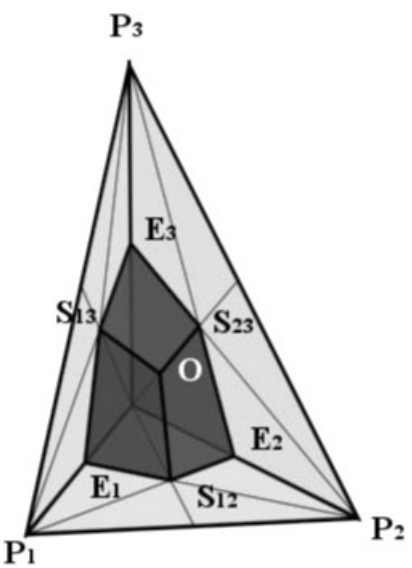

Figure 1. Geometrical layout of the cell-vertex finite volume discretization.

where the sum k runs over the control volume Ω_P obtained by joining the centres O_k with points S_{jl} and E_m. In the above, V_P is the volume of $\Omega_P = \bigcup_k \Omega_k$.

Finally, Φ_{ik} and Ξ_{ik} denote the fluxes associated with streaming and collision operators of the ith population at the kth node, respectively. Note that fluxes over the internal surfaces $\{PN_jN_l\}$ are not included because they cancel out identically (ingoing flux from a neighbour volume = outgoing flux to that same volume). Evaluation of the fluxes in Equation (4) requires knowledge of the populations f_i at the centre of the tetrahedron, edge midpoints, and centres of the surfaces. These values are obtained by the following interpolation (index k omitted for simplicity):

$$f_i(O) = \frac{f_i(P) + \sum_j f_i(N_j)}{4} \tag{5}$$

$$f_i(E_m) = \frac{f_i(P) + f_i(N_m)}{2} \tag{6}$$

$$f_i(S_{jl}) = \frac{f_i(P) + f_i(N_j) + f_i(N_l)}{3} \tag{7}$$

With these interpolation rules, the streaming fluxes read as follows:

$$\Phi_{ik} = \sum_{m=1}^{3} \sum_{l>m} \bar{f}_i(O_k, E_m, S_m l)\mathbf{c}_i \cdot \mathbf{A}(O_k, E_m, S_m l) \tag{8}$$

where bar indicates arithmetic average $\bar{f}(P,Q,R) = (f(P) + f(Q) + f(R))/3$. In the above $\mathbf{A}(P,Q,R)$ stands for the vector oriented normally to the plane surface (triangle) PQR, and magnitude equal to the area of the surface. The contribution of collisions arises from the integration of the collision term $(f_i - f_i^{\mathrm{eq}})/\tau$ over each volume Ω_k

$$\Xi_{ik} = \int_{\Omega_k} (f_i'/\tau)\,\mathrm{d}V \tag{9}$$

where $f_i' \equiv f_i - f_i^{\mathrm{eq}}$. The resulting collisional flux is computed by calculating the local non-equilibrium distribution f_i' over Ω_k via a linear interpolation. The resulting finite-volume equation takes the following general form (ULBE):

$$\partial_t f_i(P,t) = \sum_{k=0}^{K} S_{ik} f_i(P_k,t) - \frac{1}{\tau} \sum_{k=0}^{K} C_{ik}[f_i(P_k,t) - f_i^{\mathrm{eq}}(P_k,t)] \tag{10}$$

where index $k = 0$ denotes the pivotal point P. The detailed expressions of the streaming and collision matrices S_{ik} and C_{ik} are obtained by a straightforward application of the interpolation rules 5. It is readily checked that for an internal node, surrounded by a closed control volume, the following sum rules hold:

$$\sum_{k=0}^{K} S_{ik} = 0, \quad \sum_{k=0}^{K} C_{ik} = 1, \quad \forall i$$

3.1. Time marching

Time-marching proceeds according to the following sequence of explicit operator-splitting steps:

1. Streaming: $\tilde{f}_i(P, t + \mathrm{d}t) = f_i(P, t) + \frac{\mathrm{d}t}{V(P)} \sum_k \Phi_{ik}(f_i)$;
2. Update: $f_i^{\mathrm{eq}}(P, t + \mathrm{d}t)$ from $\tilde{f}_i(P, t + \mathrm{d}t)$ according to Equation (2);
3. Collide: $f_i(P, t + \mathrm{d}t) = \tilde{f}_i(P, t + \mathrm{d}t) + \frac{\mathrm{d}t}{V(P)} \sum_k \Xi_{ik}(\tilde{f}_i)$.

In two-dimensions, such time marching has been found to yield the following viscosity:

$$v = c_s^2 \tau$$

This contrasts with standard LB, which features

$$v = c_s^2 (\tau - \Delta t/2)$$

The apparently innocent shift $-\Delta t/2$ has far-reaching consequences for the computational efficiency of high-Reynolds flow simulations. To appreciate the point, let us remind that, due to the explicit treatment of the collision term, both LB and ULBE are subject to the stability constraint

$$\Delta t < 2\tau$$

Thanks to this shift (known as propagation viscosity), in LB one can achieve vanishingly small viscosities $v \sim \varepsilon$, with non-vanishing small timesteps, $\Delta t = 2\tau - \varepsilon$, still within (linear) stability constraints. Such a nice property is lost in ULBE, presumably on account of the centred interpolation used to evaluate the fluxes. The result is that the timestep required to achieve low viscosities $v \sim \varepsilon$ scales linearly with ε, thus setting a very severe restriction on the efficiency of the method for high-Reynolds flow simulations. It will be shown in the sequel that the same problem remains in 3D.

4. BOUNDARY CONDITIONS

The finite-volume procedure described above is applied to both internal and boundary nodes. However, since the control volumes of boundary nodes do not close up, additional procedures are required to handle them. Three strategies have been used to deal with boundary fluxes at wall boundaries [10, 11, 13, 14]. In this work we have used the *Covolume method*. In the covolume method, the fluxes across boundary surfaces are evaluated by explicit interpolation at the boundary surfaces (see Figure 2)

$$\Psi_i(B) = \bar{f}_i(P, E_1, S_{12}) \mathbf{c}_i \cdot A(P, \mathbf{E}_1, S_{12}) + \bar{f}_i(P, E_2, S_{12}) \mathbf{c}_i \cdot A(P, \mathbf{E}_2, S_{12})$$

For non-slip boundary conditions, the equilibrium populations at the boundary nodes are computed as local equilibria with the wall speed $\mathbf{u} = \mathbf{u}_{\mathbf{W}}$. Free-slip boundary conditions are implemented in the same way, but imposing $u_n = 0$, where u_n is the flow speed component normal to the boundary surface. The tangential component is left free. At the inlet boundary a prescribed velocity profile is imposed, whereas constant pressure is imposed at the outlet sections. Open boundaries are treated according to a straightforward three-dimensional extension

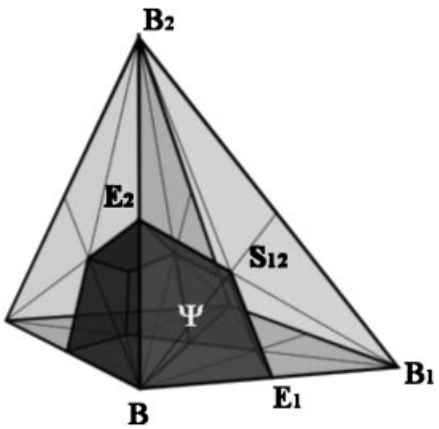

Figure 2. Geometrical lay-out for a boundary node B.

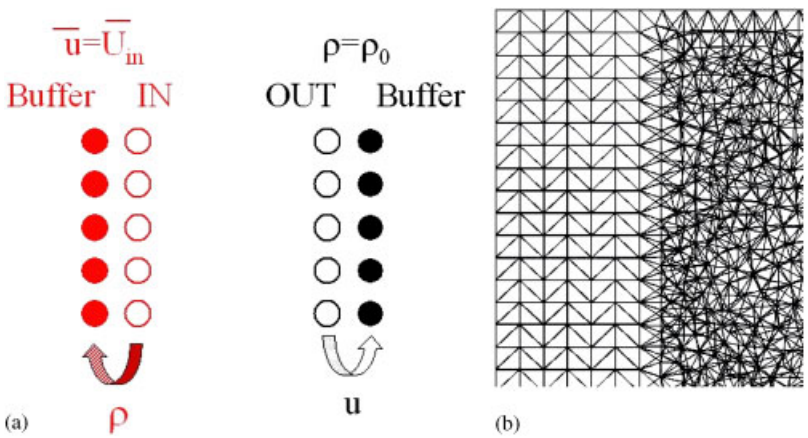

Figure 3. Inlet/outlet boundary treatment: (a) prescribed velocity (pressure) profile and zero-longitudinal pressure (velocity) gradient at inlet (outlet); and (b) buffers of uniform tetrahedra.

of the procedure developed in References [13, 14], that is by imposing the desired density and importing the velocity from the closest interior nodes. In this procedure, the computational domain is augmented with one (or more) buffers of uniform tetrahedra. The scope of these regular buffers is to ensure that the last-but-one row of nodes faces with a corresponding neighbour along the streamwise (z) direction, so that, by imposing the same value on these two rows of nodes, a zero-longitudinal-gradient boundary condition is automatically fulfilled. The three-dimensional case is more complicated because a regular cube (that is, a single cell of the standard LB) is made up by six tetrahedra.

With reference to Figure 3, inlet(outlet) boundary conditions are realized by imposing zero-longitudinal pressure(velocity) gradient condition as follows:

$$\rho(A)=\rho(I), \quad \mathbf{u}(O)=\mathbf{u}(B)$$

where $A(B)$ are the inlet(outlet) buffer nodes.

5. NUMERICAL RESULTS

In order to validate the three-dimensional ULBE technique, we have simulated two cases of practical interest: (i) pipe flow and (ii) flow past a sphere.

5.1. Pipe flow

In order to measure the numerical viscosity of the three-dimensional ULBE, we have simulated a three-dimensional laminar pipe flow. The flow is driven by a volume force, F, acting along the streamwise direction, z, with an amplitude such to produce a Poiseuille flow with a prescribed centreline speed, U_c. The geometrical parameters are $R = 7.5$ and $L = 20$ for the radial and longitudinal dimensions of the cylinder, respectively. The simulation was performed with 28 000 tetrahedra and 5400 nodes. It is to be noted that, thanks to the unstructured grid, the circular boundary is represented to a great deal of accuracy (see Figure 4). No-slip boundary conditions are applied at the cylinder surface, while periodicity is imposed at inlet and outlet sections. The kinematic viscosity was $v = 0.01$ corresponding to a centreline Reynolds number $Re_c = U_c R/v = 45$ for a Poiseuille flow with a prescribed centreline speed, $U_c = 0.06$. The numerical results are compared with the analytical solution $u_z(r) = U_c(1 - r^2/R^2)$, and the viscosity is read off from the relation $U_c = \rho F R^2/4v$.

In Figure 5 we show the longitudinal flow speed as a function of the radial coordinate. Excellent agreement with the analytical solution (solid line) is clearly visible.

Our data are consistent with the relation

$$v = c_s^2 \tau$$

which is exactly the expression found in two dimensions. This support the idea that the lack of propagation viscosity is due to centred interpolation.

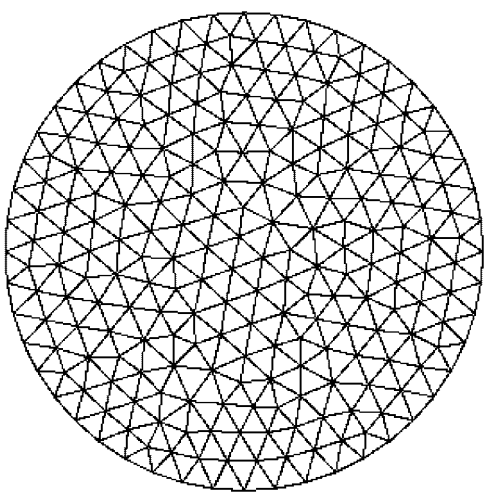

Figure 4. The irregular grid on a two-dimensional cross-flow section.

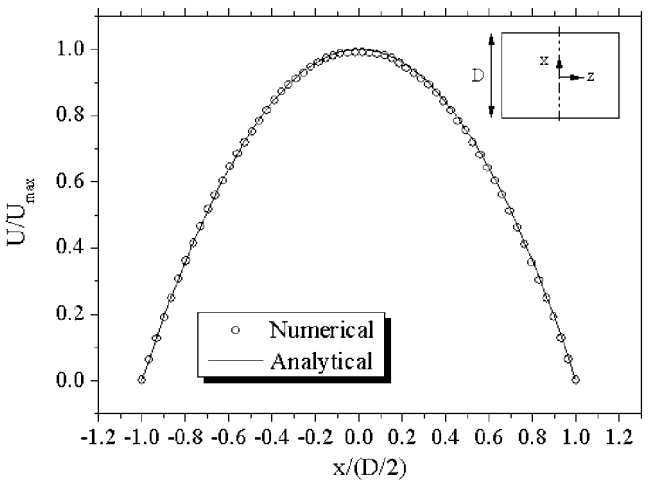

Figure 5. Parabolic Poiseuille flow: analytic versus numerical ULBE data.

5.2. *Flow past a sphere*

For the validation of the present numerical method, numerical simulations of the laminar flow past a sphere and comparisons with available literature data have been performed. Flow over a sphere has been the subject of extensive research in both experimental and numerical fluid dynamics [19–24] and, even though the geometry is very simple, it represents a hard test for a numerical code, due to the three-dimensional nature of the flow. The tests have been performed at moderate Reynolds numbers, $10 < Re < 100$, based on the free-stream velocity, U_∞, and sphere diameter, $2R_0$.

In terms of a unitary sphere radius, the channel is 30 units long and 15 units wide (square section) in order to prevent outlet and free-slip boundary conditions from affecting the flow around the sphere. The sphere is positioned at a distance of $\frac{1}{3}$ of the channel length from the inlet section.

The unstructured grids used in the computations consist of a number of nodes in the range 53 800–460 000 and 306 000–2 700 000 elements for $Re = 10$ and 100, respectively. In Figure 6 the latter grid and the coordinate system are shown. It should be noted that high density of elements in the vicinity of the spherical surface permits a highly accurate representation of the surface. This is particularly important for aerodynamic drag calculations, as it shall be detailed below. Boundary conditions are as follows: no-slip covolume method at the sphere surface, free-slip covolume method at wall boundaries and open-flow conditions at inlet and outlet sections (note additional buffers in Figure 6).

The flow is impulsively started by forcing a uniform velocity profile at inlet and imposing a prescribed pressure(density) at the outlet. Upon reaching steady-state, the drag coefficient is measured as

$$C_\mathrm{D} = \frac{2F_z}{\rho U_\infty^2 A}$$

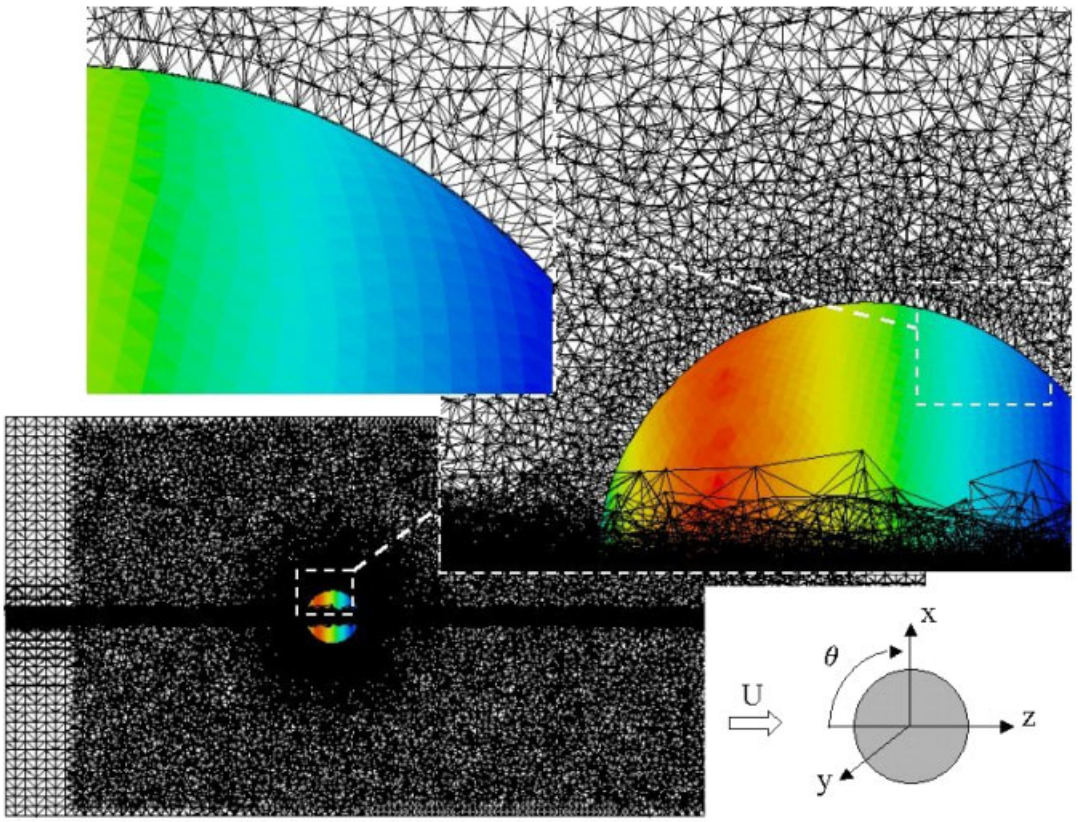

Figure 6. Coordinate system and unstructured grid near the sphere ($Re = 100$); only two 2D projections of the grid are shown.

where A is the projection area of the sphere and F_z is the streamwise component of the aerodynamic force acting on the sphere. Aerodynamic forces can be split into pressure and friction contributions. Physically, both contributions trace back to the viscosity, but this distinction is very useful from the numerical point of view because while pressure contributions are local, in a hydrodynamic (Navier–Stokes) representation, the friction contribution (viscous stress tensor) requires the computation of the velocity gradients. As observed previously, the LB approach has the useful property that the stress tensor is locally available as a linear combination of the populations. However, this property is not fully exploited in the traditional LB because the body surface does not generally lie on grid points, so that interpolations are needed at the expense of loss of accuracy [5]. The advantage of ULBE is that no interpolation is required because the body surface is fully represented by grid points. As a result, in the ULBE formulation both pressure and viscous contributions are locally available in a real sense. The numerical values of the drag coefficient, computed as discussed above, are reported in Figure 7.

From this figure, over the range 10–100 of Reynolds numbers, the calculated drag coefficients show good agreement with both numerical and experimental data [19–22].

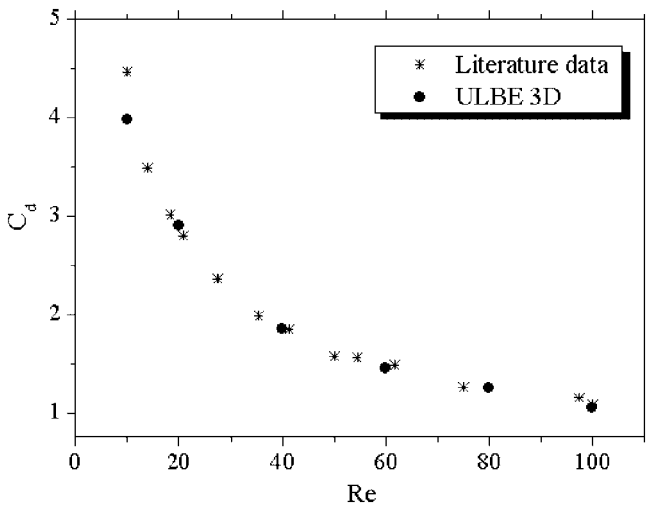

Figure 7. Computed drag coefficient at $Re = 10, 20, 40, 60, 80$ and 100: comparison with literature data [19–22].

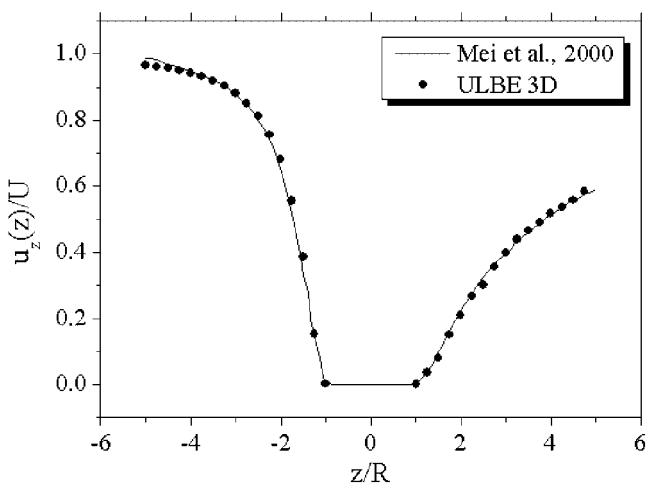

Figure 8. Flow profile $U_z(z)$ at $Re = 10$.

In Figures 8 and 9 we show the longitudinal flow speed u_z as a function of the streamwise coordinates z and y at $Re = 10$. The results compare satisfactorily with previous numerical simulations based on lattice Boltzmann formulations with curvilinear coordinates [25].

Figure 10 shows the pressure coefficient

$$C_P = \frac{2(P - P_\infty)}{\rho U_\infty^2}$$

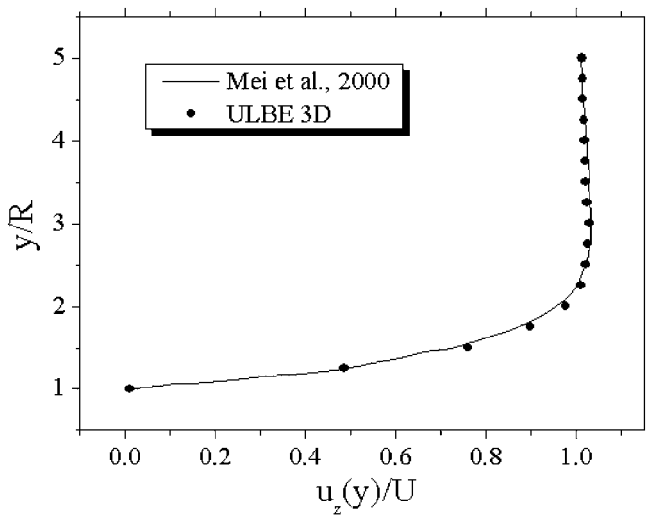

Figure 9. Flow profile $U_z(y)$ at $Re = 10$.

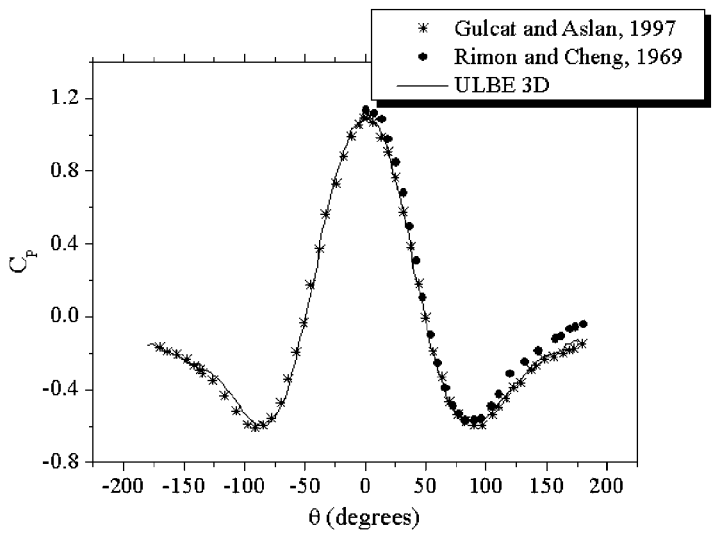

Figure 10. Comparison between the numerically calculated pressure coefficient profile and literature data [23, 24], at $Re = 100$.

as a function of the angular coordinate, θ (see Figure 6), at $Re = 100$. Again the pressure coefficient trend has been compared to numerical data found in literature [23, 24] and the agreement is excellent. In order to emphasize the sensitivity of C_P to the radial location of

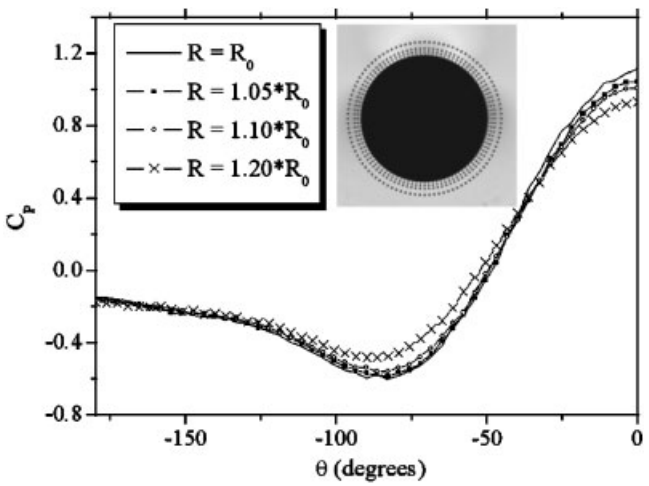

Figure 11. Pressure coefficient profile at different radial locations at $Re = 100$.

Table I. Comparison of computed results of flow past a sphere with literature data [22–24], at a Reynolds number of 100.

	[23]	[24]	[22]	Present
C_d	1	1.07	1.09	1.05
θ_s	53.5	55	52.3	54.4
l_w/D	0.86	0.93	0.87	0.92

the probes, R, this quantity is plotted as a function of θ for various radial locations R/R_0. The data in Figure 11 clearly show that a significant relative departure can be observed, depending on the radial location of the probes. This again points to the importance of locating the probes right on the spherical surface.

A very good agreement with literature data [22–24] has been also observed in terms of separation angle measured from the rear stagnation point (l_w/D) and length of the standing eddy (θ_s) measured from the base of the sphere, as shown for $Re = 100$ in Table I.

Finally, in Figure 12, we show a pictorial view of details of the flow structure past the sphere. The calculated velocity field and streamlines pattern reveal completely unsteady three-dimensional phenomena even at these low Reynolds numbers. In particular, the existence of a toroidal vortex past the sphere is clearly detected. This is in agreement with previous observations and numerical simulations [19–22]. The flow is still axisymmetric, since, as well-documented in literature [19–22], the sphere wake in a uniform flow remains axisymmetric up to a Reynolds number of about 210. Fine-scale details of microvorticity in the near-vicinity of the surface are also captured in the simulation, as shown in Figure 12.

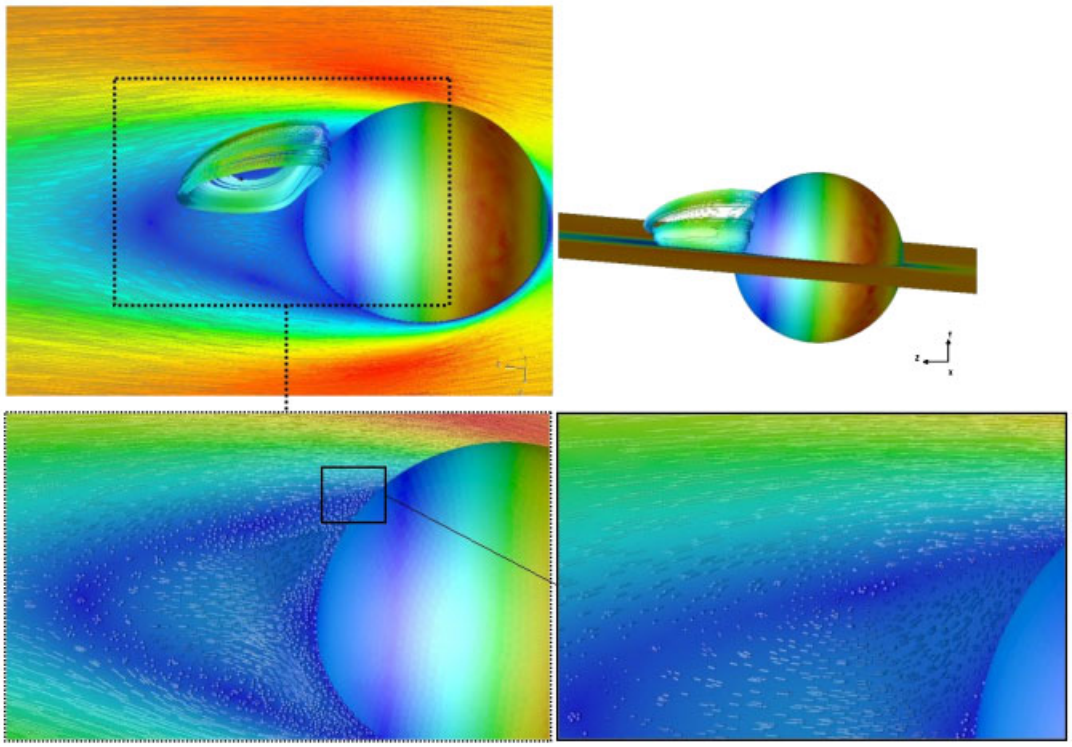

Figure 12. Different views of the velocity field and streamlines past a sphere at $Re = 100$.

6. SUMMARY AND FUTURE DIRECTIONS

Summarizing, we have extended the unstructured lattice Boltzmann method to fully three-dimensional flows.

The 3D ULBE method has been calibrated for the case of a laminar pipe flow, and successfully demonstrated for the flow past a sphere at Reynolds numbers up to $Re = 100$. Although much validation work remains to be done in order to put three-dimensional ULBE on a solid ground, the present results look encouraging. In particular, since the update of a single node takes roughly 4–5 more CPU time than for a standard LB method, computational savings are expected whenever the number of grid nodes can be reduced by, say, an order of magnitude as compared to Cartesian grids. Whether or not such a reduction can be achieved depends of course on the geometrical complexity of the problem at hand, but it is reasonable to expect that for highly complex geometries, such as, say, underhood flows for automotive applications, ULBE should indeed offer a significant potential. However, a number of limitations remain to be lifted in order to realize this potential. To date, the major limitation is the adverse scaling of the time-step with the inverse of Reynolds number. As previously discussed, this results from the lack of propagation viscosity. In order to reinstate a negative propagation viscosity, numerical interpolation should be designed so as to preserve the Lagrangian structure of the original LB space–time differencing. To the best of our knowledge, the only finite-volume

scheme which achieves this goal is the volumetric scheme of Chen [17, 18]. Unfortunately, the implementation of such a scheme for arbitrary three-dimensional geometries seems very demanding. A viable compromise may be provided by low-viscous upwind schemes. Work along these lines is currently in progress.

REFERENCES

1. Benzi R, Succi S, Vergassola M. The lattice Boltzmann equation: theory and applications. *Physics Reports* 1992; **222**:145–197.
2. Wolfe-Gladrow D. *Lattice Gas and Lattice Boltzmann Methods*. Springer: Berlin, 2000.
3. Succi S. *The Lattice Boltzmann Equation for Fluid Dynamics and Beyond*. Oxford University Press: Oxford, 2001.
4. Nannelli F, Succi S. The lattice Boltzmann equation in irregular lattices. *Journal of Statistical Physics* 1992; **68**:401.
5. He X, Shan X, Doolen G. Discrete Boltzmann equation model for nonideal gases. *Physical Review E* 1998; **57**:R13.
6. Cao N, Chen S, Jin S, Martinez D. Physical symmetry and lattice symmetry in the lattice Boltzmann method. *Physical Review E* 1997; **55**:R21.
7. He X, Luo L, Dembo M. Some progress in lattice Boltzmann method. Part I. Nonuniform mesh grids. *Journal of Computational Physics* 1996; **129**:357.
8. Filippova O, Hanel D. Grid refinement for lattice-BGK models. *Journal of Computational Physics* 1998; **147**:219.
9. Karlin IV, Succi S, Orszag S. Lattice Boltzmann method for irregular grids. *Physical Review Letters* 1999; **82**:5245.
10. Peng G, Xi H, Duncan C. Lattice Boltzmann method on irregular meshes. *Physical Review E* 1998; **58**:R4124.
11. Xi H, Peng G, Chou S-H. Finite-volume lattice Boltzmann schemes in two and three dimensions. *Physical Review E* 1999; **60**:3380.
12. Peng G, Xi H, Chou S-H. On boundary conditions in the finite volume lattice Boltzmann method on unstructured meshes. *International Journal of Modern Physics C* 1999; **10**(6):1003.
13. Ubertini S, Bella G, Succi S. Unstructured lattice Boltzmann method: further developments. *Physical Review E* 2002; **68**:016701.
14. Ubertini S. Computational fluid dynamics through an unstructured lattice Boltzmann scheme. *ASME Paper*, *IMECE2003-41194*, 2003.
15. Ubertini S, Succi S, Bella G. Lattice Boltzmann schemes without coordinates. *Philosophical Transactions of the Royal Society of London—Mathematical*, *Physical*, *and Engineering Sciences* 2004; **362**(1821):1763–1771.
16. Qian Y, d'Humières D, Lallemand P. Lattice BGK models for Navier–Stokes equation. *Europhysics Letters* 1992; **17**:479.
17. Chen H. Volumetric formulation of the lattice Boltzmann method for fluid dynamics: basic concept. *Physical Review E* 1998; **58**:3955.
18. Chen H, Teixeira C, Molvig K. Digital physics approach to computational fluid dynamics: some basic theoretical features. *International Journal of Modern Physics C* 1998; **9**:1281.
19. Dongjoo K, Choiy H. Laminar flow past a sphere rotating in the streamwise direction. *Journal of Fluid Mechanics* 2002; **461**:365–386.
20. Johnson TA, Patel VC. Flow past a sphere up to a Reynolds number of 300. *Journal of Fluid Mechanics* 1999; **378**:19–70.
21. Pruppacher HR, Le Clair BP, Hamiliec AE. Some relations between drag and low pattern of viscous flow past a sphere and a cylinder at low and intermediate Reynolds numbers. *Journal of Fluid Mechanics* 1970; **44**:781.
22. Mittal R. A Fourier–Chebyshev spectral collocation method for simulating flow past spheres and spheroids. *International Journal for Numerical Methods in Fluids* 1999; **30**:921–937.
23. Rimon Y, Cheng SI. Numerical solution of a uniform flow over a sphere at intermediate Reynolds numbers. *Physics of Fluids* 1969; **12**:949–959.
24. Gulcat U, Aslan AR. Accurate 3d viscous incompressible flow calculations with the fem. *International Journal for Numerical Methods in Fluids* 1997; **25**:985–1001.
25. Mei R, Luo L-S, Shyy W. An accurate curved boundary treatment in the lattice Boltzmann method. *Journal of Computational Physics* 1999; **155**:307.

